Fuel 413 (2026) 138208

Contents lists available at ScienceDirect

Fuel

journal homepage: www.elsevier.com/locate/jfue

Full length article

Numerical investigation of methanol-air mixture formation and combustion in a dual-fuel marine engine at low load

Giang Bùi [a], Konstantinos Zoumpourlos [b,*], Cemil Bekdemir [c], Bart Somers [a]

[a] Eindhoven University of Technology, Groene Loper 5, 5612 AE, Eindhoven, The Netherlands
[b] Delft University of Technology, Mekelweg 2, 2628 CD, Delft, The Netherlands
[c] TNO, Automotive Campus 30, Helmond, 5708 JZ, The Netherlands

HIGHLIGHTS

- Full cylinder multi-cycle CFD simulations using high pressure methanol PFI.
- BR above 65% is not recommended at low load due to low efficiency and partial burn.
- Delaying SOI by 60 CA generally lowers efficiency and NOx, but increases CO.
- Injecting more methanol from the short runner improves mixture homogeneity and burning rate.

ARTICLE INFO

Keywords:
Methanol combustion
Port fuel injection (PFI)
Marine dual-fuel engine
CFD
Mixture formation

ABSTRACT

Port fuel injection (PFI) methanol-diesel dual-fuel is considered a promising retrofit solution for methanol adoption in marine engines. PFI enables fuel flexibility, improved thermal efficiency, and reduced greenhouse gas (GHG), soot, and NOx emissions. This work aims to provide insights for the optimization of PFI methanol-diesel marine engines, contributing to the decarbonization of the maritime sector. For this purpose, Computational Fluid Dynamics (CFD) simulations in CONVERGE-CFD are performed, incorporating spray modeling and combustion kinetics of both methanol and diesel to investigate high-pressure PFI methanol behaviours injected at different locations.

The developed CFD model satisfactorily captured methanol-air mixture formation and methanol combustion under low-load dual-fuel operation measured at 3.1 bar Brake Mean Effective Pressure (BMEP). Two distinct phases of dual-fuel combustion are captured: compression ignition of n-heptane, as a surrogate for diesel, and fast flame propagation of premixed methanol, with results being sensitive to blending ratio (BR), start of injection (SOI), and injector location. At 3.1 bar BMEP, varying BR between 45%–65% yielded increased combustion efficiency (91.9%–94.8%) and gross Indicated Thermal Efficiency (ITE) (46.2%–47.3%), while BRs above 75% caused partial burn and efficiency drop. Advancing SOI improved mixture uniformity and flame propagation rate, however, it increased NOx and heat release rate of the second phase. Injecting more methanol from the short runner promoted homogeneity, raising combustion efficiency by up to 8%-points, thermal efficiency up to 4.3%-points, and NOx emissions by 50%. These results highlighted the model's capability to simulate dual-fuel operation and advance the understanding towards efficient and low-emission methanol marine engines.

1. Introduction

In the marine industry, internal combustion engines (ICEs), using fossil fuels such as diesel and heavy fuel oil, remain the dominant technology for propulsion [1]. Therefore, to achieve the International Maritime Organization (IMO)'s ambitious target of net-zero greenhouse gas (GHG) emissions from ships by 2050 [2], the adoption of alternative fuels with low to zero carbon content is of great interest. Among alternative fuels for ICEs in maritime transport, methanol (CH_3OH) has emerged as a promising replacement for petroleum-based ones [3]. This is due to methanol's higher volumetric energy density compared to other alternative fuels such as hydrogen and ammonia [4]. Its liquid state at atmospheric conditions also simplifies storage and distribution onboard

* Corresponding author.
Email address: k.zoumpourlos@tudelft.nl; kon.zoumpourlos@gmail.com (K. Zoumpourlos).

https://doi.org/10.1016/j.fuel.2025.138208
Received 20 October 2025; Received in revised form 18 December 2025; Accepted 28 December 2025
Available online 6 January 2026

[5]. Moreover, methanol's heating value and volumetric energy content are less than half of those of conventional fuels like diesel, while having a significantly high heat of vaporization (1100 kJ/kg, compared to 250 kJ/kg of diesel) [6,7]. This challenges methanol-air mixture formation by inducing a charge cooling effect, which reduces in-cylinder temperatures throughout the engine cycle [8]. Accordingly, lower wall heat loss, reduced NOx emissions, and improved resistance to engine knock are expected. The evaporative cooling effect increases charge densities; therefore, it increases volumetric efficiency, which can offset the low volumetric energy content [4].

Methanol is well-suited for spark ignition (SI) engines due to its high octane rating [9]. On the contrary, methanol is resistant to auto-ignition and has a very low cetane number compared to diesel. This hinders the application of methanol as the marine sector mainly relies on CI engines. To tackle methanol's poor ignition properties, port fuel injection (PFI) dual-fuel (DF) technology has been developed extensively [10]. In PFI mode, a low reactivity fuel, e.g., methanol, is injected into the intake port directed at the intake valve. Then, the air-fuel charge is ignited by a small amount of high reactivity fuel, e.g., diesel, which is directly injected (DI) into the cylinder. This strategy is often regarded as an ideal retrofit solution due to its low cost, fuel flexibility, improved thermal efficiency, and potential to reduce GHG, soot, and NOx emissions [11].

Previous studies revealed low NOx and soot emissions and high thermal efficiency at increased blending ratio (BR) of methanol in PFI DF engines. Wang et al. [12] showed that the cylinder conditions do not intersect with the area of high NOx and soot formation in the equivalence ratio-temperature (φ-T) map at BR of 80%. This explains the decrease in both NOx and soot emissions of dual-fuel engines. Among four DF modes with BR in the range of 30% – 80%, the highest brake thermal efficiency (BTE) and lowest CO, NOx, and soot emissions were achieved at 80% BR [13]. In another numerical investigation of a large-bore medium-speed marine engine [14], port methanol injection at 50% BR can reduce NOx emissions by 30.5% compared to diesel-only mode. According to an experimental study on a six-cylinder marine engine [15], at BR of 60.6%, brake specific fuel consumption (BSFC) of DF mode was 15.6 g/(kWh) lower and BTE was about 3%-points higher than the baseline diesel engine.

In PFI methanol – DI diesel mode, the upper limit of BR depends heavily on engine load. Four operating bounds that constrain maximum BR at different operating loads were identified by Wang et al. [16]. These are partial burning and misfire at low to medium load, and roar combustion and knocking at high to full load. In the viable operating range, the maximum BR is 76% at 43.5% engine load [16]. Li et al. [17] found that at low load, BR is limited to 30% due to inefficient combustion while at high load, BR of methanol can reach up to 50% with delayed diesel injection and increased EGR to reduce knock intensity. The simulation results by Karvounis et al. [14] also revealed an upper limit of 50% BR for PFI mode due to increased in-cylinder pressure and unstable combustion. A study on a retrofitted high-speed marine engine by Dierickx et al. [11] indicated the maximum BR of 54% at high load which can be extended to 70% at mid load. From the experimental investigation by Cung et al. [18], longer ignition delay, higher carbon monoxide (CO) and HC emissions were observed with increasing BR at low loads, while an increased peak of pressure rise rate restricted BR at high loads. At 75% load, a maximum BR of 49.4% was achieved by retarded injection timing of renewable diesel [18].

Once injected into the intake port, methanol sprays break up, evaporate, and mix with air. The formation of a flammable methanol-air mixture is often challenging due to methanol's high lower flammability limit and large heat of vaporization. Yet the mixing quality of methanol with air is crucial for its ignition in the cylinder, especially at high BR where the combustion system relies on premixed flame propagation. The simulation results in [19] indicated that mixture homogeneity can be improved with optimized injection strategies, e.g., injection window within intake stroke and matching injection pressure and SOI of methanol. The experimental results in the same study showed that BTE of a heavy-duty SI methanol engine was promoted with better mixture homogeneity due to shortened combustion duration and methanol lean burn [19]. Delayed SOI of methanol after intake valve opening (IVO) led to more homogeneous and lower in-cylinder mixture temperature, increasing BTE and reducing both HC and CO emissions [20]. In contrast to [19,20], Singh et al. [21] suggested that good homogeneity levels can be achieved with advanced injection timing such that injection ends close to IVO. Regarding methanol combustion, numerical results indicated the sensitivity of flame propagation to the quality of mixture formation [21].

In contrast to SI engines, the mixture formation issue of the PFI methanol has rarely been addressed in DF mode. Sun et al. [22] conducted multi-cycle simulations of a medium-speed marine engine operating in diesel-methanol dual-fuel (DMDF) mode. It was concluded that advanced injection timing (SOI at −440 CA ATDC), increased nozzle diameter (0.3 mm), and increased methanol injection pressure (20 bar) minimized mass of liquid film, improving fuel economy and ITE [22]. As indicated in a numerical study by Mousavi et al. [23], the revised design of the intake manifold, in which methanol injectors are angled toward the intake valve, effectively reduced the methanol mass imbalance among cylinders to 3%. Simulations also demonstrated that injection timing, injection duration, and nozzle location can substantially impact methanol mass distribution [23].

1.1. Aim & novelty

Previous experimental studies on methanol-diesel dual-fuel (DF) engines have primarily examined the effects of increasing methanol blending ratios, with limited attention to injection timing or the evaporation and mixing processes [13,16,18,24]. Numerical investigations typically assume a perfectly premixed methanol-air charge in the intake manifold, enabling axisymmetric simulations of only part of the cylinder [12,14,17,25]. Consequently, spray dynamics and the influence of port fuel injection (PFI) on atomization, evaporation, and mixing are often neglected. In this work, we focus on marine sized engines, which are often larger compared to the small-bore engines (below two liters displacement volume) analyzed in prior work [11,17,26–28]. Studies on DF marine engines with large cylinders remain scarce, particularly under high methanol blending conditions. Moreover, unlike previous studies using low methanol injection pressures (3–10 bar), we employ a high-pressure methanol injection system to improve mixture formation at high blending ratios. PFI DF offers flexibility in injector placement, including pre- or post-intercooler positions [26], single-point injection (SPI) in the intake pipe [11], and multi-point injection (MPI) at the intake ports. While prior research explored these strategies [11,26,29], MPI configurations were limited to one injector per cylinder without investigating alternative positions or multiple injectors per port.

To address the presented literature gaps, this work investigates the effects of PFI methanol on the mixing and combustion of a 4-liter dual-PFI single-cylinder high-speed marine engine at low load using computational fluid dynamics (CFD) simulations. The novelty of the presented approach lies in a full cylinder marine engine model incorporating state-of-the-art spray modeling coupled with air-fuel mixture formation, and combustion using detailed chemistry. The model was developed in CONVERGE-CFD, and incorporates the spray framework which was extensively validated in the past work of the authors with methanol-dedicated data allowing for predictive mixing studies [8,30,31]. Thus, by not assuming a perfectly homogeneous methanol mixture, our study leverages the full engine cylinder geometry to account for the localized air-fuel distribution, and model methanol-diesel combustion more realistically. Our work strongly contributes to improving our understanding of contemporary methanol-diesel marine engines, aiming to achieve the sustainability goals of the maritime sector.

The paper is structured as follows. First, the CFD model, which incorporates the injection and combustion of both methanol and diesel, is set up in Section 2 and validated for diesel-only and dual-fuel conditions in Section 3. The mixture formation analysis is then conducted

to explore the evaporation, wall wetting, and mixing processes of the reference dual-fuel case. Finally, the model is used to study the impact of methanol injection settings, such as injection amount, timing, and location, on engine performance and emissions in Section 4.

2. Numerical methodology and setup

2.1. Experimental and computational configurations

A three-dimensional simulation model of the methanol-diesel engine was established using CONVERGE v3.1. The CFD model was validated using measurements from the single-cylinder engine setup at TNO. More details on the single cylinder experimental setup can be found in Kiouranakis et al. [32]. The main specifications of the tested engine are listed in Table 1. A methanol injector is installed at each intake runner, where the fuel spray is directed towards the cylinder along the air path. One diesel injector is installed at the center of the cylinder head for diesel DI. The computational domain representing the experimental setup is shown in Fig. 1.

The computational grid is generated automatically at every time step by CONVERGE. The base grid size is 8 mm with fixed embedding in certain regions of the domain and adaptive mesh refinement (AMR) based on velocity and temperature. A 2 mm cell size is applied to refine the grid near the piston, cylinder head, and along the liner throughout the simulation time; 1 mm within the intake and exhaust manifolds; and 0.5 mm around the valve bottom during valve movement. With respect to the injector nozzles, the grid is refined in a conical area with a size of 0.5 mm during the injection window. Similarly as in the authors' previous spray modeling work [30], a small cylinder embedding is included around the nozzles of each injector to accurately resolve the air-entrainment in the jet. When AMR is implemented, the cell sizing in the cylinder and intake runners can reach 0.5 mm, if the absolute value of the sub-grid velocity field or temperature field exceeds 1 m/s or 2.5 K, respectively. The maximum number of cells in the computation time is approximately 2.5 million.

Table 1
Testing engine specifications.

Items	Specification
Number of cylinder	1
Bore (mm)	170
Stroke (mm)	180
Displacement (L)	4
Compression ratio	14
Speed (rpm)	1500
Number of nozzles per methanol injector	6
Methanol nozzle diameter (mm)	0.197
Number of nozzles per diesel injector	10
Diesel nozzle diameter (mm)	0.270

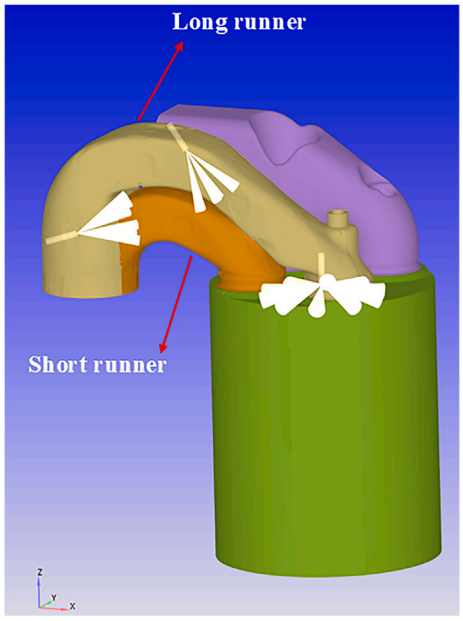

Fig. 1. Computational domain with injector locations.

2.2. Computational models

The finite volume approach with a second-order accurate spatial scheme has been used to numerically solve the conservation equations of the fluid flow. In addition, the Redlich-Kwong equation of state (EOS) was chosen for compressible flows to couple density, pressure, and temperature. In the transient solver, the first-order implicit Euler method was used for time advancement with variable time-step control based on the Courant-Friedrichs-Lewy (CFL) criterion [33].

Additional sub-models have been implemented to capture the respective physical phenomena including turbulence, multiphase flow and combustion. The Re-normalization Group (RNG) k-ϵ model [34] was utilized to predict the turbulent flow. For the multiphase flow modeling, the discrete phase modeling method [33] was used, in which parcel (liquid droplets) motion is tracked in a Lagrangian frame of reference, while the gaseous phase is represented in an Eulerian frame. The fuel droplets are introduced into the domain using the Blob injection model [35], where the injected drop size is equal to the nozzle diameter. Moreover, the Kelvin Helmholtz – Rayleigh Taylor (KH-RT) model [36] was employed to simulate the primary and secondary breakup of the spray. The interaction of spray droplets through collisions and coalescence was modeled using the No Time Counter (NTC) scheme [37] and Post Collision Outcome [38]. The Kuhnke film splash model [39] was chosen to account for the interaction of liquid drops with solid surfaces.

The evaporation process of droplets and liquid film was calculated using Frossling and film vaporization models [33], respectively. The film vaporization model assumes a uniform temperature distribution within the wall film. The temperature of the film is calculated by following the energy balance between four energy terms on the wall: convection to the gas, vaporization of the film mass, conduction from the wall, and boiling of the film. The sub-models for spray modeling in this study are summarized in Table 2. The aforementioned sub-models have been applied to examine the characteristics of PFI methanol sprays under relevant conditions for marine engines [30,31].

Regarding combustion modeling, the SAGE detailed chemical kinetics solver was used to solve detailed combustion chemistry [33]. This solver requires a kinetic mechanism file that describes the elementary reactions. To simplify combustion and emissions modeling, n-heptane (nC_7H_{16}) was chosen as the single-component diesel surrogate since its cetane number (CN = 56) is very close to that of diesel (CN = 53) [40]. Although n-heptane does not capture all combustion-related physio-chemical properties—such as those critical for soot modeling compared to complex multi-component surrogates—it provides accurate ignition delay, enabling reliable prediction of dual-fuel combustion. Notably, diesel liquid properties were assigned to the spray parcels,

Table 2
Sub-models for liquid droplets lifetime.

Droplets Phenomena	Numerical models
Droplet injection	Blob model [35]
Droplet breakup	KH-RT model [36]
Droplet collision	No Time Counter model [37]
Droplet coalescence	Post Collision Outcome model [38]
Spray/wall interaction	Kuhnke model [39]
Droplet evaporation	Frossling model [33]
Liquid film evaporation	Film Evaporation model [33]

while n-heptane was used to represent the gaseous phase. Moreover, the mechanism of Liu et al. [41] was adopted, which consists of 52 species and 182 reactions, for methanol/n-heptane dual-fuel combustion. Lastly, the extended Zel'dovich mechanism [42] was used to simulate NOx formation.

2.3. Reference case description

Previous studies [43–46] showed that the combustion characteristics and engine performance of methanol-diesel mode are sensitive to the injection of diesel. As the ignition source, diesel combustion is crucial for controlling the ignition and premixed combustion of methanol in the cylinder. Therefore, the first validation case for the CFD model is for the diesel-only operating condition. From the experiments of the engine setup, the low load point was chosen since the diesel injection mass is similar to that in the dual-fuel mode.

The respective operating conditions of diesel-only and methanol-diesel dual-fuel simulation cases are presented in Table 3. Parameters such as temperature, pressure, mass of fuel injected, BR, and λ_{MeOH} in those conditions are extracted from the experimental measurement points at TNO, and used as input in the CFD models. Furthermore, the methanol injection window relative to valve timing is illustrated in Fig. 2. The injection amount and timing are similar between the two methanol injectors. For all cases, the methanol injection pressure was kept constant at 140 bar, while the SOI is at the crank angle before firing TDC. In the engine setup, solenoid injectors were used for methanol injection, delivering a precise amount of fuel at specific timing. On the other hand, diesel was injected using a mechanically driven injector with a fixed injection timing.

2.4. Simulation analysis parameters

This section describes the parameters used to indicate mixing quality, combustion characteristics, and efficiency. To quantify the amount of diesel replacement with methanol, blending ratio (BR) is defined on an energy basis as shown in Eq. (1).

Table 3
Operating conditions for reference case of diesel-only and dual-fuel mode.

Parameters	Case 1-D	Case 1-DF
BMEP [bar]	1.3	3.1
$m_{inj,diesel}$ [mg]	63.4	47.2
$m_{inj,methanol}$ [mg]	0	121.7
BR [%]	0	55
λ_{MeOH}	6.1	6.6
T_{intake} [K]	298.7	353.1
P_{intake} [kPa]	114.1	120
$T_{exhaust}$ [K]	469.5	570.1
$P_{exhaust}$ [kPa]	116.5	124.5

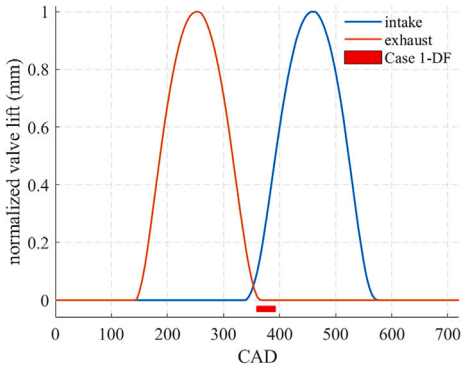

Fig. 2. Injection window (rectangle bar) in relation to valves timing.

$$BR = \frac{\dot{m}_{CH_3OH} \cdot LHV_{CH_3OH}}{\dot{m}_{CH_3OH} \cdot LHV_{CH_3OH} + \dot{m}_{diesel} \cdot LHV_{diesel}} \cdot 100\%, \quad (1)$$

where $\dot{m}$ and LHV denote the mass flow rate and lower heating value of fuel, respectively.

To assess mixture homogeneity inside the cylinder, the standard deviation of air-fuel equivalence ratio (λ_{std}) was used, and calculated as follows [33]:

$$\lambda_{std} = \sqrt{\frac{\sum_{cell} m_{cell}(\lambda_{cell} - \lambda_{mean})^2}{m_{total}}}, \quad (2)$$

where m_{cell} is the cell mass, λ_{cell} is the λ within a cell, λ_{mean} is the average λ in the cylinder, and m_{cell} is the total mass in the cylinder. High values of λ_{std} imply a high degree of inhomogeneity.

Combustion efficiency $\eta_{combustion}$ was calculated as follows:

$$\eta_{combustion} = \frac{Q_{chemical}}{Q_{fuel}}, \quad (3)$$

where $Q_{chemical}$ is the heat released from reactions and $Q_{fuel} = m_{diesel} * LHV_{diesel} + m_{methanol} * LHV_{methanol}$ is the total fuel energy. In the simulation, $Q_{chemical}$ is the total chemical heat release, calculated by CONVERGE.

The gross or net indicated thermal efficiency (ITE) can be calculated using the following equation:

$$ITE_{gross/net} = \frac{W_{gross/net}}{Q_{fuel}}, \quad (4)$$

where $W_{gross/net}$ is the indicated gross or net work, computed by CONVERGE based on pressure data in one full cycle.

3. Reference case validation & analysis

3.1. Diesel-only case – combustion

To justify the CFD setup and the use of n-heptane as a surrogate in dual-fuel simulations, the diesel-only case D-1 was simulated, validating our approach using measurements at a low load operating point as shown in Table 3. Fig. 3 shows the comparison of in-cylinder pressure and apparent heat release rate (AHRR) between experiment and simulation. The numerical results of in-cylinder pressure and AHRR generally agree well with measured values, despite a small underestimation of 1.5 bar in the peak cylinder pressure. In addition, according to the AHRR curve in Fig. 3, almost all of the injected fuel is consumed in a premixed combustion mode which ends by 2 CAD.

Regarding combustion phasing, CA05 is predicted 0.1 CA earlier, while the simulated CA50 is delayed by 1.4 CA compared to the experiment. This indicates a well predicted ignition delay time (defined as

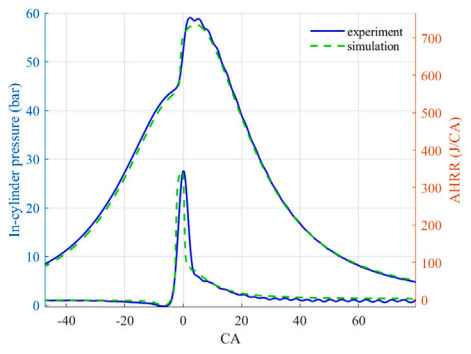

Fig. 3. Comparison between numerical and experimental in-cylinder pressure and AHRR of case 1-D.

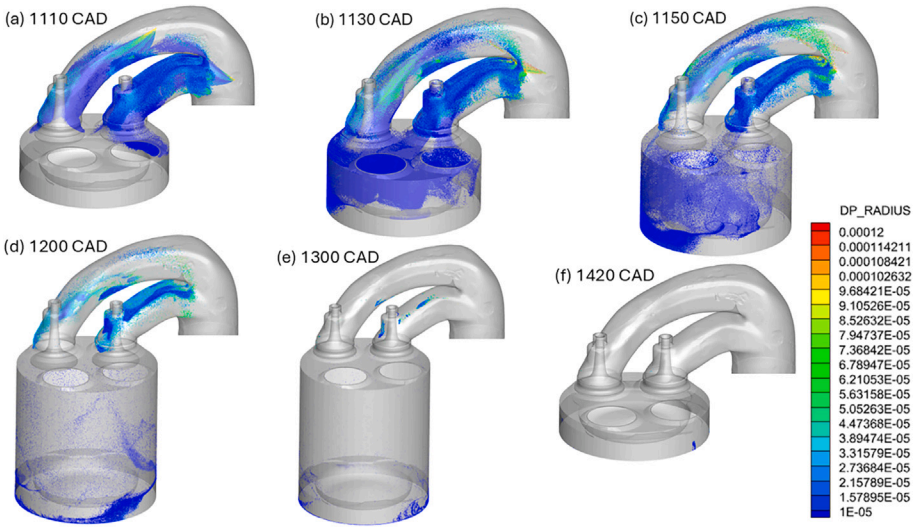

Fig. 4. Evolution of parcels radius, case 1-DF. Note: the exhaust manifold is removed from the contours to give a better view of the spray in the intake runners.

the interval between SOI and CA05), and a slightly retarded combustion phasing (defined as the timing of CA50) by the CFD model. Based on the presented validation results, the CFD model can accurately predict the ignition timing and main combustion event of diesel using n-heptane. Therefore, the same approach will be applied for the DI of n-heptane in dual-fuel simulations where n-heptane ignites the premixed methanol.

3.2. Dual-fuel case – mixture formation

In this section, the results pertinent to the methanol mixture formation in the reference dual-fuel case are presented. The evaporation process of methanol in case 1-DF is illustrated through the mass of methanol vapor and the history of parcel radius. To reach equilibrium, multi-cycle simulations were conducted to stabilize the wall film mass and obtain the desired in-cylinder methanol mass. Moreover, the total amount of methanol vapor does not vary between the second and third cycle, implying that equilibrium is reached at the third cycle, see Fig. 5. Thus, the evolution of the injected methanol at the third cycle is provided and discussed below.

The spatial distribution of the film and parcels is better illustrated by the 3D droplet radius contours in Fig. 4. Initially, spray from the long runner injector hits the wall due to its orientation, and part of the short runner spray hits the junction between the two runners and then flows directly into the long runner. This upward movement of parcels from the short runner injector is driven by the momentum of inlet airflow. As the formed liquid spray structure is bent upwards, many parcels impinge on the upper part of the short runner, increasing the mass of liquid film after the end of injection (EOI). The remaining part of the spray from both runners is directed towards the cylinder, reducing the mass of liquid parcels in the runners while raising the liquid fuel amount in the cylinder. After reaching its peak around EOI, methanol in liquid form, e.g., parcels and film, gradually decreases to 2 mg in total at IVC. This is attributed to the residual liquid methanol in the runners experiencing a long period of 182 CA between EOI and IVC. Hence, both thermal conduction with the wall and thermal convection from the intake air play important roles in its evaporation. Notably, at 20 CA before TDC, no liquid methanol exists in the domain.

As can be seen from Fig. 5, around 30% of the methanol evaporates within the injection window. This initially evaporated methanol concentrates near the liquid film in the runners, eventually flowing into the cylinder following the downward motion of intake valves, see Fig. 6(a)–(c). During the first cycle, after EOI, the total evaporation amount continues to rise up to approximately the injection amount at 20 CAD before TDC. In the second and third cycle, the total mass of methanol vapor exceeds the injection amount by 3 mg due to the residual gaseous methanol in the intake runners from the previous cycle. The majority (96%–97%) of gaseous methanol is inside the cylinder at 20

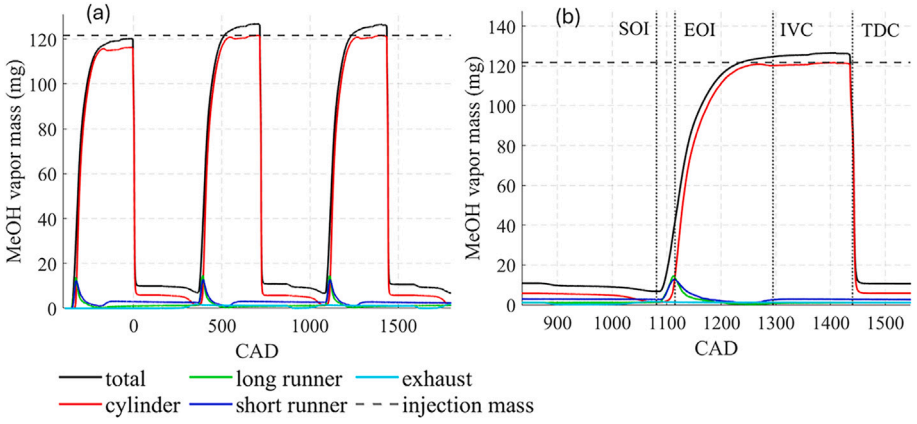

Fig. 5. Amount of methanol vapor (a) across three cycles and (b) at the 3rd cycle, case 1-DF.

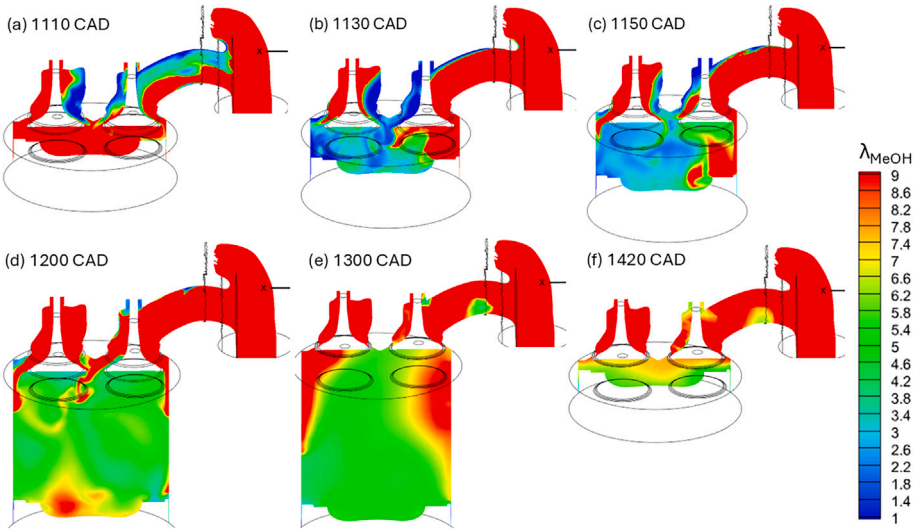

Fig. 6. Distribution of λ_{MeOH} across the intake valves, case 1-DF.

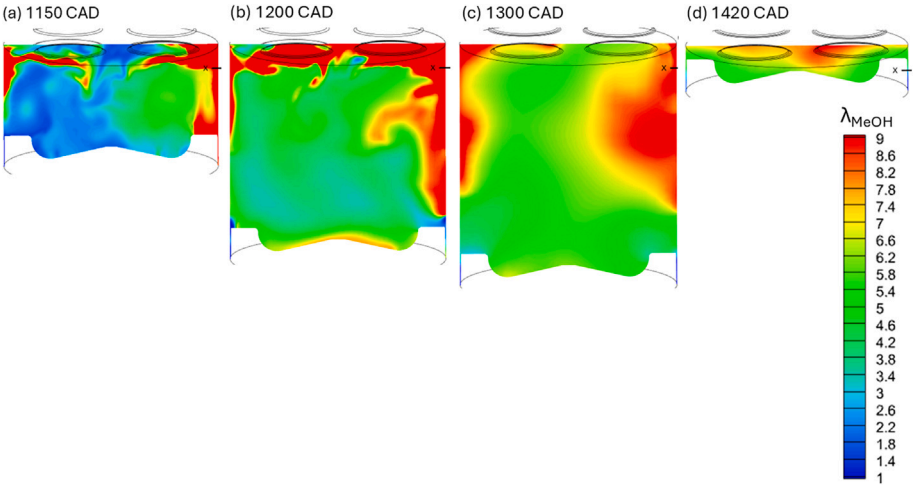

Fig. 7. Distribution of λ_{MeOH} in the cylinder, case 1-DF.

CAD before TDC. Hence, it is concluded that from the second cycle, all of the injected methanol evaporates and enters the cylinder in gaseous state.

Although the majority of the fuel evaporates, the in-cylinder mixture after EOI is relatively inhomogeneous with richer regions around the piston bowl and the long runner valve, see Figs. 6(b) and (c) and 7 (a). During the rest of the intake stroke, as the piston moves downwards and the evaporation amount increases, the fuel-air mixing is promoted under swirl and crossflow inside the cylinder. After IVC, the methanol-air mixture is uniform except for very lean regions along the liner as demonstrated in Figs. 6(e) and 7(c). As illustrated in Figs. 6(f) and 7(d), the homogeneity is improved at the end of the compression stroke due to the squish of the piston. The average in-cylinder λ_{MeOH} at 20 CAD before TDC is 6.2. However, it is not distributed evenly across the cylinder with a leaner region of $\lambda_{MeOH} = 7 - 8.6$ close to the center of the cylinder head, surrounded by a moderately richer region of $\lambda_{MeOH} = 5 - 6.6$ adjacent to the bowl and liner.

3.3. Dual-fuel case – combustion

The mixture formation results indicate that at the 3.1-bar BMEP operating point, the mass of gaseous methanol available for combustion and the average in-cylinder λ_{MeOH} are in correspondence with expectations based on measurements. Therefore, as the next step, the validation of dual-fuel combustion in case 1-DF will be presented here. As can be seen from Fig. 8(a), the simulated pressure in the cylinder matches very well with the measurements, except for a 3.1 bar overestimation of the peak pressure. The discrepancy between numerical and experimental pressure is less than 1 bar during compression and less than 0.5 bar during the expansion stroke, while the error during the combustion event is within 5%.

Furthermore, similarly to the experiment, the simulation result exhibits two peaks in the AHRR, representing two phases of combustion. The first combustion phase is the compression ignition of the pilot fuel, which completely consumes n-heptane before TDC, presented in Fig. 8(b). Fig. 9 illustrates the combustion of n-heptane which ignites a part of methanol in the core of the n-heptane jet. The subsequent burning phase, indicated by the second peak, combusts the majority of methanol within 20 CA after TDC. Fig. 10 demonstrates the rapid consumption of methanol in the second phase, characterized by fast flame propagation within the premixed fuel-air. Both peaks of numerical AHRR are overpredicted compared to the experimental data, implying a higher burning rate computed by the CFD model. This might be due to larger chemical heat release computed from the kinetics mechanism.

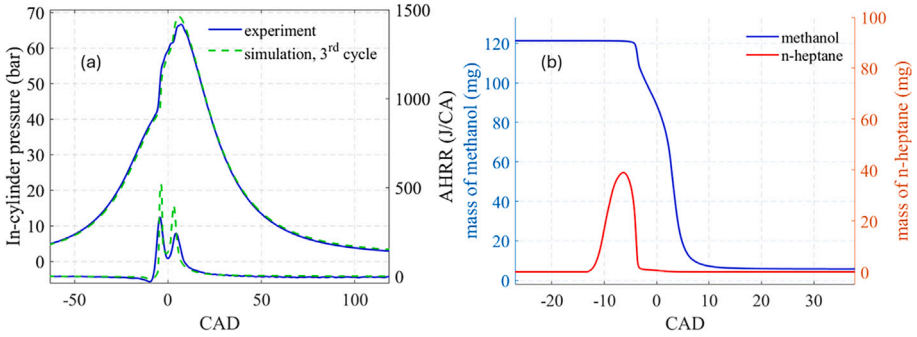

Fig. 8. (a) Comparison between numerical and experimental in-cylinder pressure and AHRR of case 1-DF (b) Mass of both fuels in the cylinder around TDC.

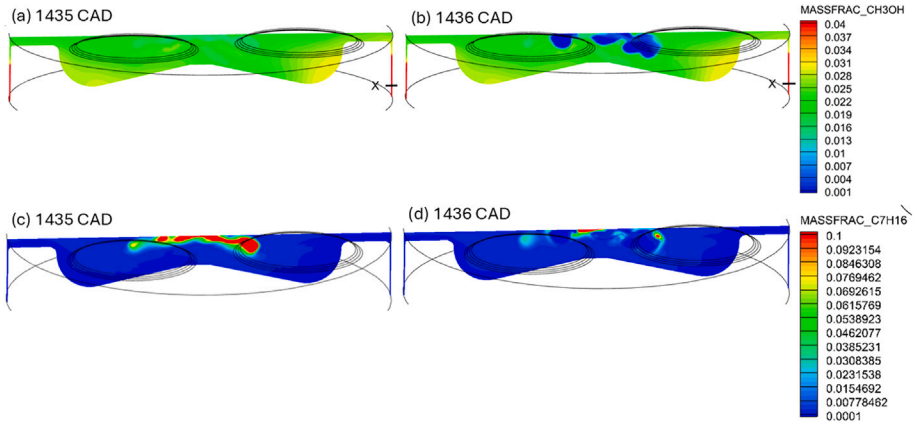

Fig. 9. (a) and (b) Mass fraction of methanol at ignition; (c) and (d) Mass fraction of n-heptane at ignition.

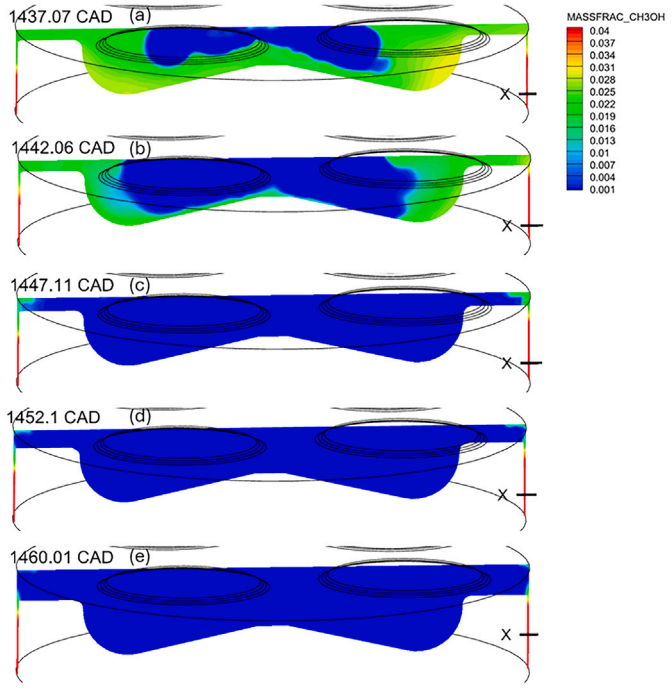

Fig. 10. Consumption of methanol following the ignition.

With respect to combustion phasing, CA05 and CA10 from simulation are slightly delayed by 1.12 and 0.84 CA compared to the experiment, respectively. However, combustion phasing (CA50) and end of combustion (CA90) occur earlier by 0.83 and 2.92 CA, respectively. Hence, the numerical combustion duration is about 4 CA shorter than the measured value of 25.25 CA. In fact, the simulated ITE_{gross} and ITE_{net} are 46.24% and 43.53% respectively, about 5.4%-points higher than the experimental values. Better thermal efficiency may stem from higher combustion efficiency and/or lower wall heat loss predicted by the simulation.

In conclusion, despite the overestimation of peak cylinder pressure and burning rate in the later combustion phase, the overall combustion characteristics are acceptably captured by the CFD model under the presented operating conditions. Combined with the satisfactory prediction of the mixture formation, the currently validated CFD model was used in parametric studies to investigate the effects of methanol injection on mixing and combustion in the dual-fuel engine.

4. Methanol injection studies

As discussed in 3.2 and 3.3, mixture formation from simulation provides a combustible mixture that exhibits an overall good agreement in terms of experimental pressure and heat release at 3.1 bar BMEP load. Therefore, the validated CFD model has been used to investigate the effects of methanol injection on mixing and dual-fuel combustion under the same operating condition. Three variations regarding methanol injection amount (Blending Ratio sweep), timing (SOI sweep), and

Table 4
Ratio to total amount injected and λ_{MeOH} in five cases of BR 45%–85%.

BR	% over $m_{inj,methanol}$	λ_{MeOH}
45	99.8	7.55
55	99.8	6.20
65	100.3	5.19
75	100.9	4.48
85	105.7	3.84

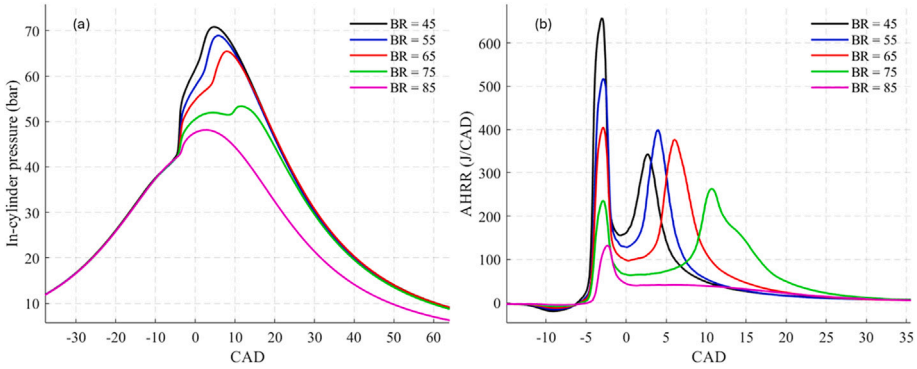

Fig. 11. (a) In-cylinder pressure and (b) AHRR in five cases of BR 45%–85%.

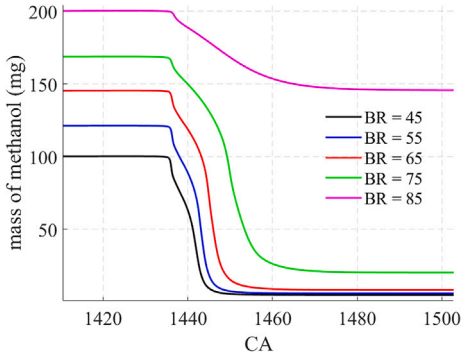

Fig. 12. Evolution of in-cylinder methanol mass at the third cycle in five cases of BR 45%–85%.

location (injection amount split between two injection locations) are simulated using the case 1-DF as the reference simulation. The previous sections show that the steady state is reached by the third cycle. Hence, the results and analyses corresponding to the third cycle of each variation will be presented below.

4.1. BR sweep

Within the injection amount variation, BR is swept from 45% to 85% in intervals of 10%. Besides satisfying the BR value, the injection amounts of n-heptane and methanol in each case are calculated such that the total fuel energy is the same as in the reference case. The injection duration of methanol is adjusted based on the injection amount so that the injection pressure is 140 bar in each case. The rest of the modeling inputs remain the same as in the reference case.

Regarding methanol evaporation, the liquid parcels and the wall film follow the same behavior as in case 1-DF. Specifically, liquid parcels and film mass increase immediately after SOI, reach their peak at around EOI, and decrease to almost zero towards TDC. Thus, the mass of methanol vapor available for combustion in each case is very close to the injection amount, as shown in Table 4. In cases BR 65, 75, and 85%, the gaseous methanol amount even exceeds the injection mass due to residual methanol in the cylinder from the previous cycle, see Fig. 12.

As observed in Fig. 11(a), the rate of pressure rise following the ignition decreases at higher BR. Peak pressure is lowered by 17.5 bar and delayed by 6.8 CA as BR increases from 45% to 75%. In the case of the highest BR of 85%, there is only one phase of pressure rise, in contrast to the two-phase pressure rise—characterized by a second, steeper pressure gradient in the other four cases. The trend of in-cylinder pressure is consistent with the AHRR at varied BR, see Fig. 11(b). For the BR 45%–75% cases, two peaks of AHRR indicate two combustion phases, namely compression ignition of n-heptane and fast premixed flame propagation of methanol. The heat release of the initial burning phase is dominated by the combustion of n-heptane. Since the injection mass of n-heptane is larger at lower BR, the first AHRR peak is highest in case of BR 45% (657.8 J/CA) and reduces at higher BR (517.7, 405.1, and 236.1 J/CA at BR 55, 65, and 75%, respectively). As BR increases from 45% to 75%, the second combustion phase is more delayed than the first one, indicating a slower burning rate.

The final cumulative heat release of three cases BR 45%, 55%, and 65% is comparable, while that of BR 75% is about 296.2 – 367 J lower. This is because the unburned methanol at BR 75% is about 2.5 – 4.3 times higher compared to BR 45%, 55%, and 65%, as shown in Fig. 12. Opposite to lower BR, the flat, prolonged tail of AHRR after the first peak at BR 85% implies partial burning of the methanol in the cylinder. Specifically, only 27.4% of methanol vapor is consumed after combustion in the third cycle at BR 85%. Since the case BR 85% shows undesired

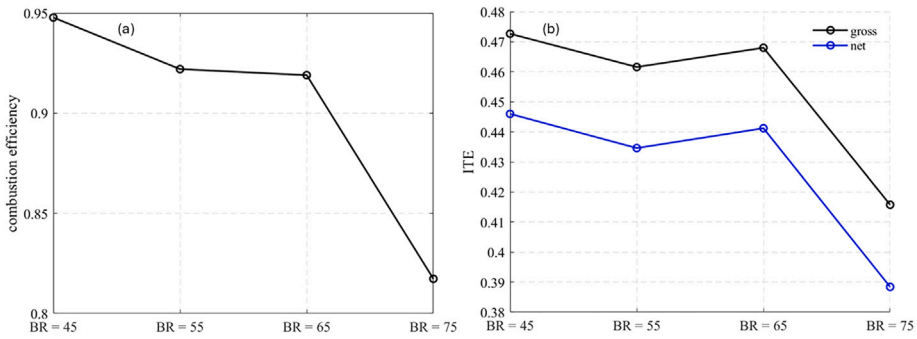

Fig. 13. (a) Combustion efficiency and (b) Indicated thermal efficiency in four cases of BR 45%–75%.

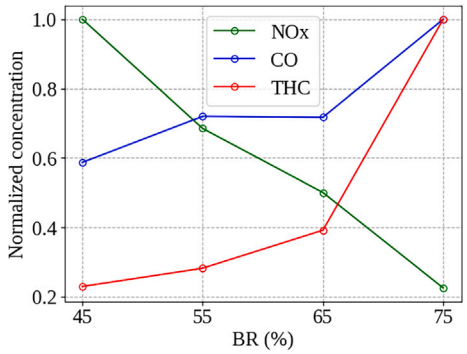

Fig. 14. Normalized concentration of major emissions species in four cases of BR 45%–75%.

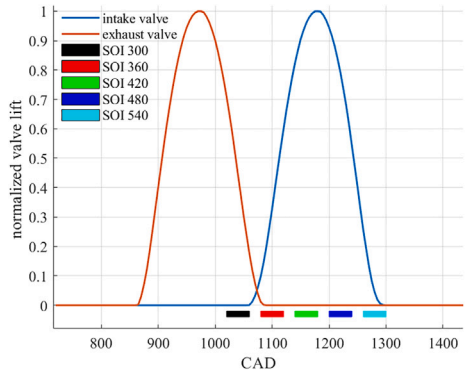

Fig. 15. Injection window relative to normalized valves timing.

combustion characteristics with a large amount of unburned methanol, it will not be discussed further.

Combustion duration in cases BR 45%, 55%, and 65% is very similar, ranging between 20.2 – 21.4 CA. However, combustion duration at BR 75% is about 4.2 – 5.4 CA longer with a larger interval between the first and second burning phases seen in Fig. 12. It is due to higher BRs creating more intense cooling effects which hinder ignition and flame propagation. More rapid combustion and lower residual fuel mass denote better combustion efficiency. This is demonstrated by Fig. 13(a) with combustion efficiency in cases BR 45%, 55%, and 65% between 91.9% and 94.8%, which is 10.2%–13.1%-points higher compared to case BR 75%. In addition, as observed in Fig. 13(b), the difference in thermal efficiency among cases BR 45%, 55%, and 65% is minimal, with η_{gross} between 46.2%–47.3% and η_{net} between 43.5%–44.6%. Thus, the present single cylinder setup could potentially be expanded up to BR 65% under low load operation while maintaining adequate combustion performance.

Although emissions values have not been validated for the reference case, the trend of some emissions is of interest to show nevertheless. Therefore, the normalized concentration of main emissions species is compared among four BR 45%–75% in Fig. 14. The amount of CO and unburned hydrocarbon (THC) are lower in the case of better combustion efficiency. For example, CO and THC concentration at BR 75% is 1.7 and 4.4 times larger than that at BR 45%, respectively. On the other hand, the concentration of NOx reduces almost linearly with increasing BR, dropping by 4.2 times as BR increases from 45 to BR 75%.

In summary, at the presented low load condition, increasing BR reduces NOx significantly due to the higher amount of methanol available for combustion. Due to methanol's evaporation cooling effect, the in-cylinder mixture temperature is lower, resulting in lower NOx emissions. However, in this operating condition, for BRs higher than 65%, combustion efficiency deteriorates and a large amount of methanol remains unburned. Besides larger replacement by methanol, the mass of n-heptane decreases as BR increases to keep total energy input approximately constant. Thus, the combustion of the reduced n-heptane amount at very high BR only ignites a limited region near the jet and does not generate sufficient thermal energy to sustain the flame propagation. This leads to partial burn or even misfire, worsening the combustion and thermal efficiency. Among three cases at lower BR, considering favorable combustion characteristics, good efficiency, and low emissions, BR 65% is chosen for the following methanol injection investigations.

4.2. SOI sweep

In this section, a sensitivity analysis on the SOI of the BR 65% case was performed. Here, the start of methanol injection is varied such that the injection window is within the intake valve opening event, except for one case with very early timing. Fig. 15 presents the injection timing of each case relative to the valves' timing, with SOI listed in the legends. The other modeling parameters are kept the same as case BR 65% and the reference case. This section will discuss the mixture formation and combustion of these cases to study the effects of methanol injection timing in dual-fuel mode.

In simulation cases with SOI 300 and 360 CAD, the methanol evaporation behavior is similar to the case 1-DF discussed in 3.2. With early SOI, the amount of evaporated methanol quickly rises after SOI and approaches the injection amount close to TDC at the second cycle, see Fig. 16(a). For SOI at 300 and 360 CAD, after the second cycle, all of the injected methanol in each cycle evaporates and enters the cylinder to form a flammable methanol-air mixture.

For SOI at 420 and 480 CAD, in-cylinder vapor mass in the first cycle is 77.2% and 32.8% of the injection mass, respectively. Late injection timing leaves a large part of the injected methanol in the runners after IVC, which enters the cylinder when the intake valves open in the next

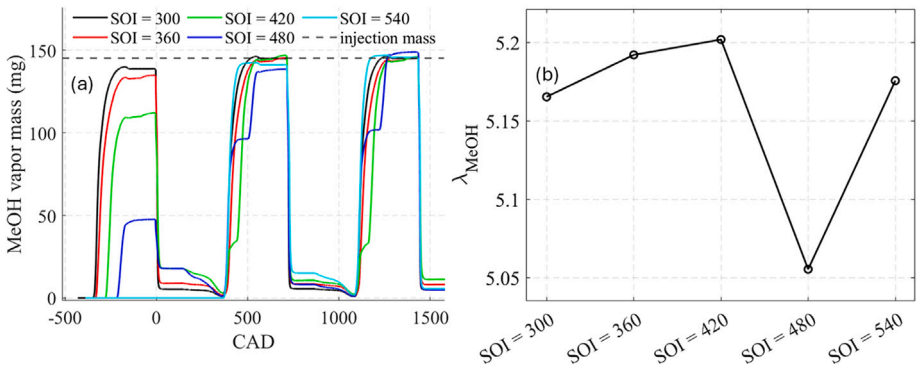

Fig. 16. (a) Amount of in-cylinder methanol vapors across three cycles and (b) Average in-cylinder λ_{MeOH} at 1420 CAD in five cases of SOI 300 – 540 CAD.

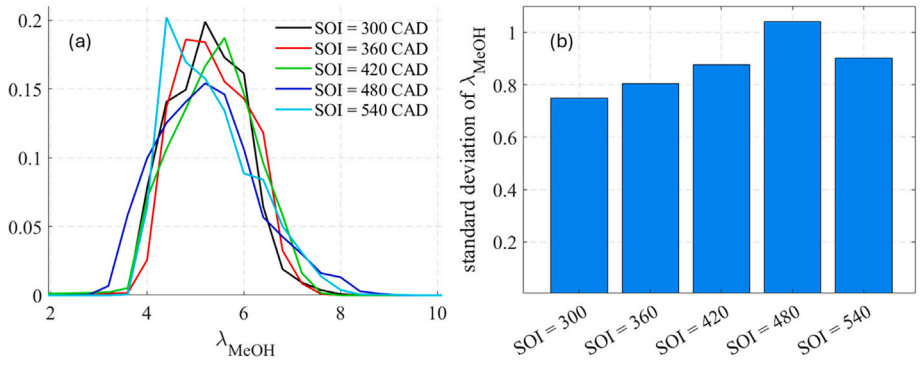

Fig. 17. (a) Mass-weighted histogram and (b) Standard deviation of in-cylinder λ_{MeOH} at 1420 CAD in five cases of SOI 300 – 540 CAD.

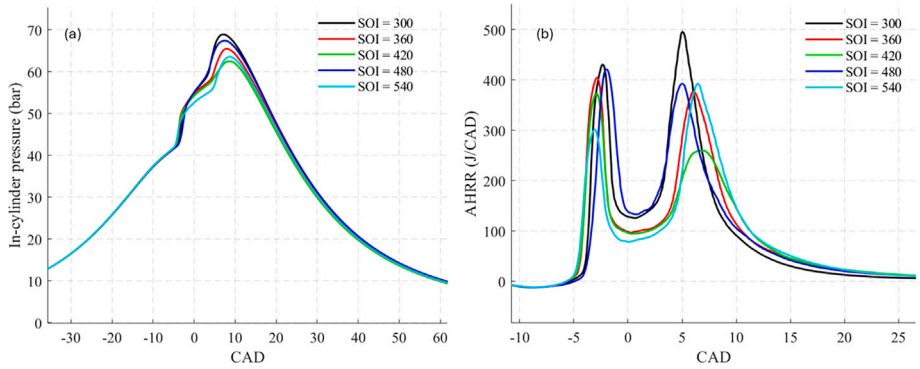

Fig. 18. (a) In-cylinder pressure and (b) AHRR in five cases of SOI 300 – 540 CAD.

cycle. This results in an initial increase in vapor mass after IVO in the second and third cycles. This is followed by a sharp rise in the evaporation amount as the new injection starts.

In case of SOI 540 CAD, no methanol vapor is found in the cylinder during the first cycle, as injection ends after IVC and there is insufficient time for vapor transfer. Gaseous methanol remains in the runners before flowing into the cylinder after IVO of the subsequent cycle. At 1420 CAD, the in-cylinder vapor mass is 145–145.9 mg for SOI 300–540 CAD, except for SOI 480 CAD, which is slightly higher at 148.9 mg. This leads to lower λ_{MeOH} by about 0.1–0.14 in case of SOI 480 CAD as presented in Fig. 16(b). At 1420 CAD, the mass-weighted histogram in Fig. 17(a) shows similar λ_{MeOH} ranges (3.6–8) for SOI 300–420 and 540 CAD, while SOI 480 CAD exhibits a moderately wider range (3.2–8.4). Hence, standard deviation of in-cylinder λ_{MeOH} in case of SOI 480 CAD is minimally larger by 0.1 – 0.3, indicating a slightly more inhomogeneous mixture close to TDC compared to the other four cases.

Fig. 18 shows a similar trend in in-cylinder pressure and AHRR curve among five cases SOI 300 – 540 CAD. Two gradients of pressure rise denote two combustion phases, also indicated by two peaks of AHRR. The heat release rate of the first phase in case SOI 300 CAD is comparable to case SOI 480 CAD, but is larger by 103.2 J/CAD at its second peak. The faster burning rate in the second phase of combustion for SOI at 300 CAD may be due to better homogeneity of methanol-air mixture in the cylinder. This characteristic is also observed between cases SOI 360 and 420 CAD. In all cases, the majority of methanol available for combustion (92.3%–96.5%) is consumed.

The simulation results reveal a shorter ignition delay, later phasing, and longer combustion duration as SOI is retarded by 60 CA, except for SOI at 480 CAD. Based on Fig. 19, for SOI between 300 and 420 CAD, combustion and thermal efficiency decrease by 4% and 2%-points as SOI is delayed by 60 CA, respectively. However, combustion efficiency increases by almost 10%-points and ITE by 4.5%-points when SOI is

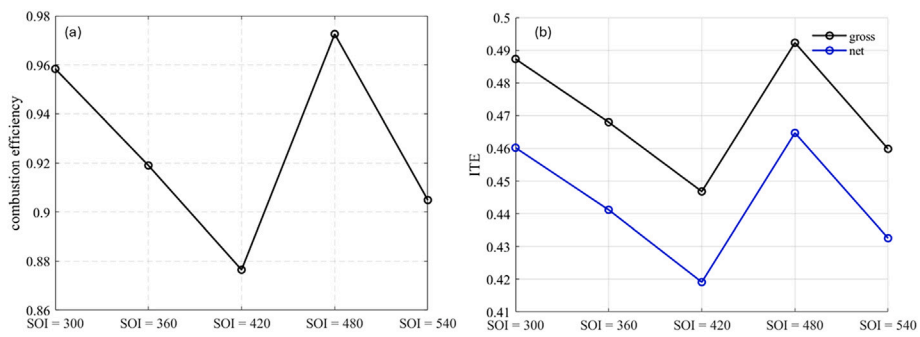

Fig. 19. (a) Combustion efficiency and (b) Indicated thermal efficiency in five cases of SOI 300 – 540 CAD.

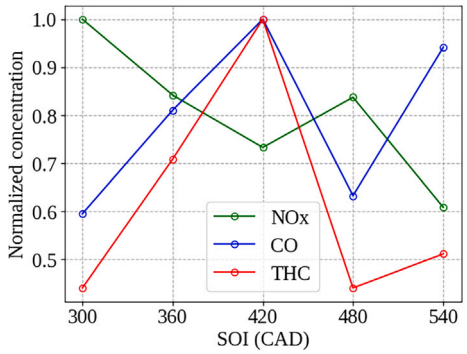

Fig. 20. Normalized concentration of major emissions species in five cases of SOI 300 – 540 CAD.

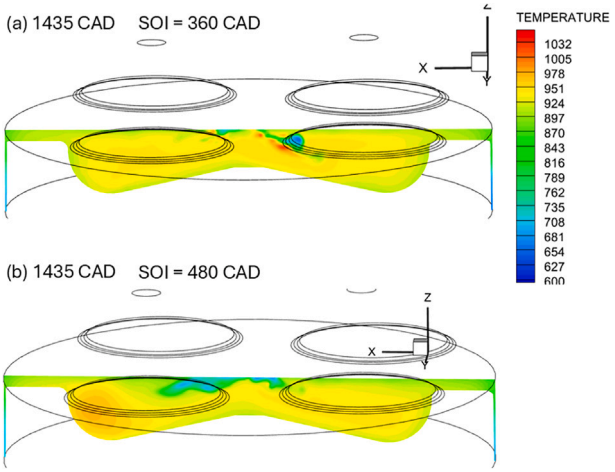

Fig. 21. Temperature field prior to ignition (1435 CAD) for SOI at 360 CAD and 480 CAD.

retarded from 420 to 480 CAD, before decreasing again by 6.7%-points and 3.2%-points at SOI 540 CAD, respectively. The trend disruption at SOI 480 CAD is also observed in the normalized concentration of major emission species plotted in Fig. 20. It should be noted that the reported emissions were not rigorously validated, as our intention is to compare trends among the different cases. CO and THC emissions in case SOI 480 CAD approximate those in case SOI 300 CAD, while NOx only rises up to case SOI 360 CAD level.

To explain the exception in combustion characteristics of case SOI 480 CAD, the in-cylinder temperature and methanol mass fraction in cases SOI 360 CAD and 480 CAD were compared during ignition and main combustion event. Fig. 21 illustrates the high-temperature region adjacent to n-heptane jet for SOI at 360 CAD and near the piston bowl for SOI at 480 CAD before ignition. Therefore, ignition delay is shorter in case SOI 360 CAD compared to SOI 480 CAD. As can be seen from Fig. 22, methanol concentration in case SOI 480 CAD is larger close to the cylinder head. This is in line with lower average λ_{MeOH}, denoting a slightly richer methanol-air mixture for SOI at 480 CAD as presented in Fig. 16(b). Contours of methanol mass fraction also indicate faster propagation of premixed methanol within 10 CA after TDC. This is because of higher temperature in the unburned region, particularly close to the piston bowls in case SOI 480 CAD, see Fig. 23.

To sum up, in case SOI 480 CAD, enhanced burning rate in the second combustion phase results in shorter combustion duration, better efficiency, and lower CO and THC emissions. However, mixture inhomogeneity, longer ignition delay, and increased NOx emissions are the drawbacks of such late injection timing. Besides, the case with SOI at 480 CAD limits the injection duration to end before IVC, which is important in cases where the injection amount varies. Very early SOI at 300 CAD induces homogeneous mixture, good efficiency, low CO and THC emissions. On the contrary, it also leads to the highest NOx emissions among five cases, due to the increased combustion temperature. Additionally, the flame propagation phase during the second AHRR peak increases rapidly and exceeds the first peak. Hence, to balance efficiency, emissions, combustion stability, and flexibility in adjusting injection amount, the simulation case with SOI at 360 CAD was used in the last injection study to investigate the injection location.

4.3. Injection location

In the previous cases, the injection amount was split evenly between two injectors in the long and short runner. To examine the influence of injection location on mixing and combustion, the injection mass at each injector was varied from 0% to 100% from the short runner in steps of 25%. The rest of the numerical settings remained the same as the reference case, which has BR 65% and SOI at 360 CAD.

The evaporation amount at 1420 CAD is comparable among five cases and close to the total injection mass (145.13 mg ± 1.9%). In case of 100% injection from the short runner, the vapor mass is slightly smaller

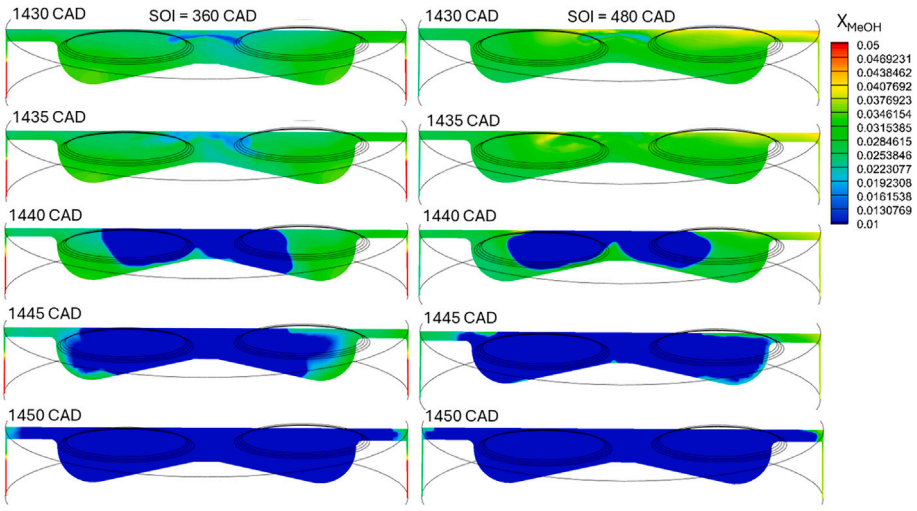

Fig. 22. Distribution of methanol mass fraction in the cylinder from 1430 to 1450 CAD for SOI at 360 CAD and 480 CAD.

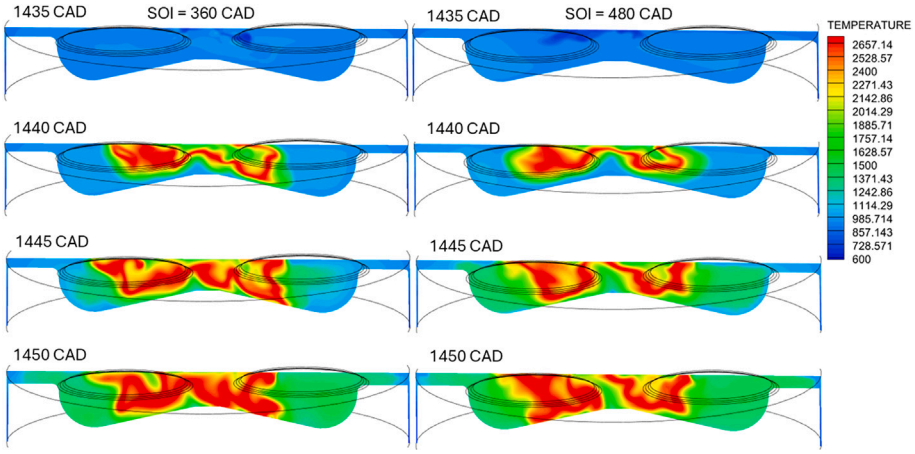

Fig. 23. Temperature field in the cylinder from 1435 to 1450 CAD for SOI at 360 CAD and 480 CAD.

by 2.8 mg compared to the injection mass due to a large amount of liquid film that remained in the runners. Vapor mass exceeds injection amount in case of equal injection and 25% from short runner due to residual gas from the previous cycle and the evaporation from liquid parcels in the cylinder. The average in-cylinder λ_{MeOH} prior to n-heptane injection is also similar across the five cases, falling within a narrow range of 5.2–5.3. The mass weighted histogram and standard deviation of λ_{MeOH} at 1420 CAD in Fig. 24 indicate improved mixture homogeneity with larger injection mass in the short runner case.

Based on in-cylinder pressure and AHRR presented in Fig. 25, the cases with increased injection amount from the short runner exhibit a faster burning rate. This is illustrated through the higher pressure gradient and larger heat release rate in the second combustion phase. In cases of 50%–100% of total injection mass from the short runner, the second AHRR peak occurs about 2.2 – 2.7 CA earlier and reaches 134.9 – 209.2 J/CAD higher compared to the two cases with larger injection from the long runner. More rapid combustion during flame propagation of the premixed methanol phase can be associated with better homogeneity for cases 50%–100% short runner as discussed above.

Fig. 26 demonstrates that combustion efficiency is enhanced by 6.6%–8%-points and ITE by 3.3%–4.3%-points. According to the trends reported by the normalized concentrations in Fig. 27, low concentrations

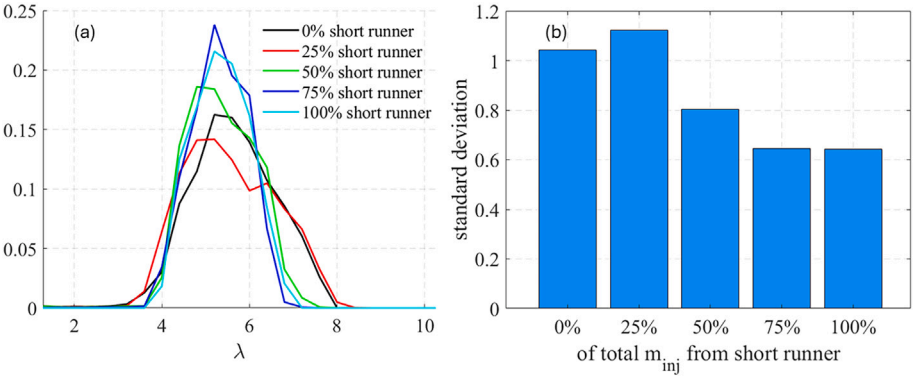

Fig. 24. (a) Mass-weighted histogram and (b) Standard deviation of in-cylinder λ_{MeOH} at 1420 CAD in five cases of injection location.

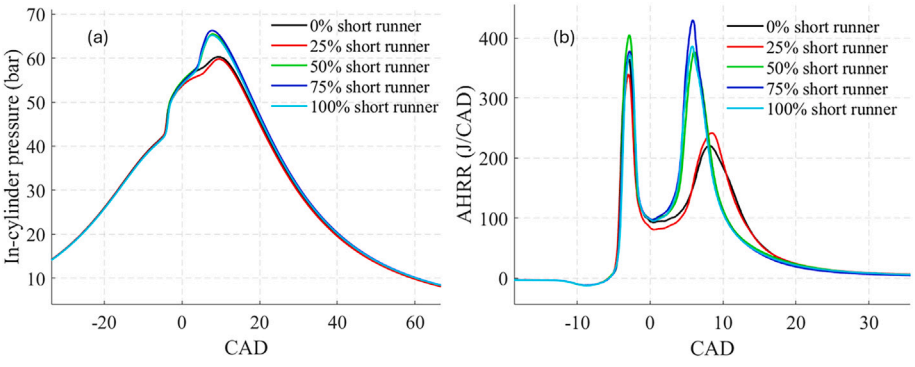

Fig. 25. (a) In-cylinder pressure and (b) AHRR in five cases of injection location.

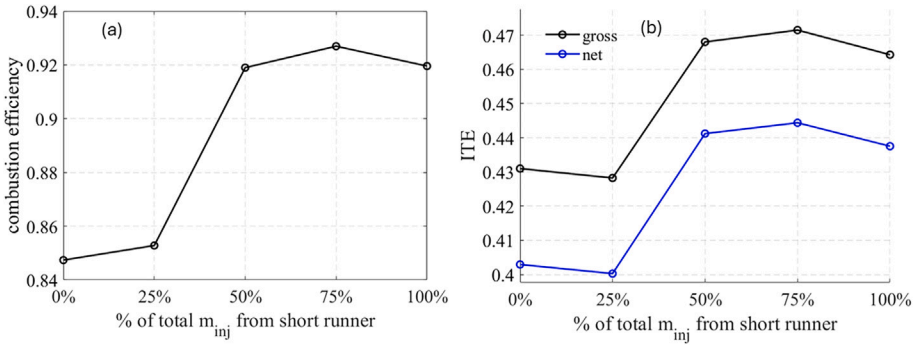

Fig. 26. (a) Combustion efficiency and (b) Indicated thermal efficiency in five cases of injection location.

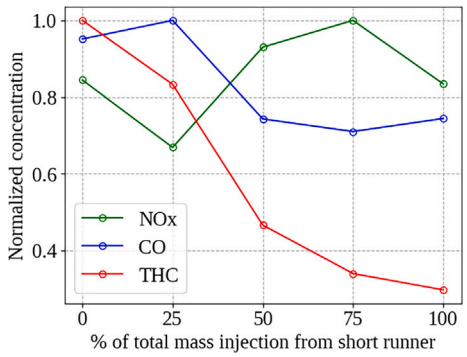

Fig. 27. Normalized concentration of major emissions species in five cases of injection location.

of CO and THC are found in cases with high combustion efficiency. When the injection amount from the short runner increases from 25% to 75%, NOx concentration rises by 1.5 times. However, when injecting fully from either runner, NOx emissions remain at a similar level.

To understand the enhanced mixture homogeneity and faster combustion with more injection mass from the short runner, mixture formation and combustion process of cases 75% and 25% short runner were analyzed. As observed in Fig. 28, liquid parcels spread throughout the cylinder between 1120 and 1160 CAD. In contrast, liquid parcels are mostly present in the in-cylinder regions underneath the intake valve connected to the long runner as shown in Fig. 29. For brevity, the part of the cylinder below the intake valve connected to the long runner will be called the left side, and that below the short runner will be referred to as the right side. When entering the cylinder, droplets from the long runner injector disperse mainly on the left side, while those from the short runner injector distribute equally on both sides. This is because the short runner jet is tilted upwards under the effect of the intake air stream, causing part of the spray to travel along the upper wall of the runner and be directed toward the left side of the cylinder. On the other hand, the long runner jet follows the intake airflow direction, concentrating its droplets on the left side. Besides faster droplet evaporation, the even distribution of droplets in the cylinder improves mixture homogeneity in the case of 75% of the total injection amount from the short runner, as illustrated in Fig. 30. For 25% of the total injection amount from the short runner case, after EOI, the localized droplets spread to the right side due to the swirl motion. Consequently, droplets evaporate slowly and in a non-uniform way, leading to an inhomogeneous methanol-air mixture close to TDC, as shown in Fig. 31.

Fig. 32 demonstrates faster methanol consumption in the case of 75% short runner. Due to a highly uniform mixture, the propagation of premixed methanol is almost identical on both sides of the cylinder. In contrast, the propagation in the 25% short runner case is asymmetrical with a faster rate on the left side, which contains a leaner methanol-air mixture. As presented in Fig. 33, the temperature field is nearly even in case of 75% short runner injection, while the temperature near the piston

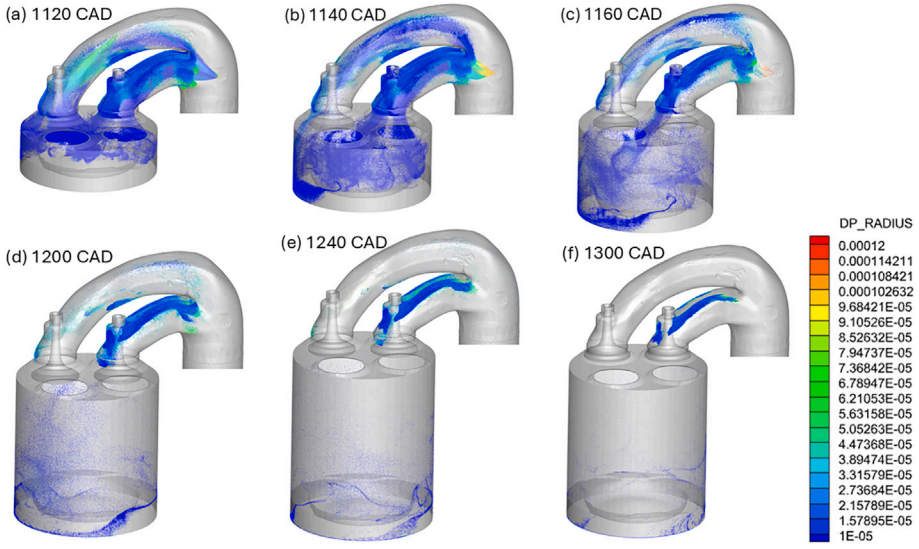

Fig. 28. Evolution of parcels radius in case 75% of total injection amount from short runner.

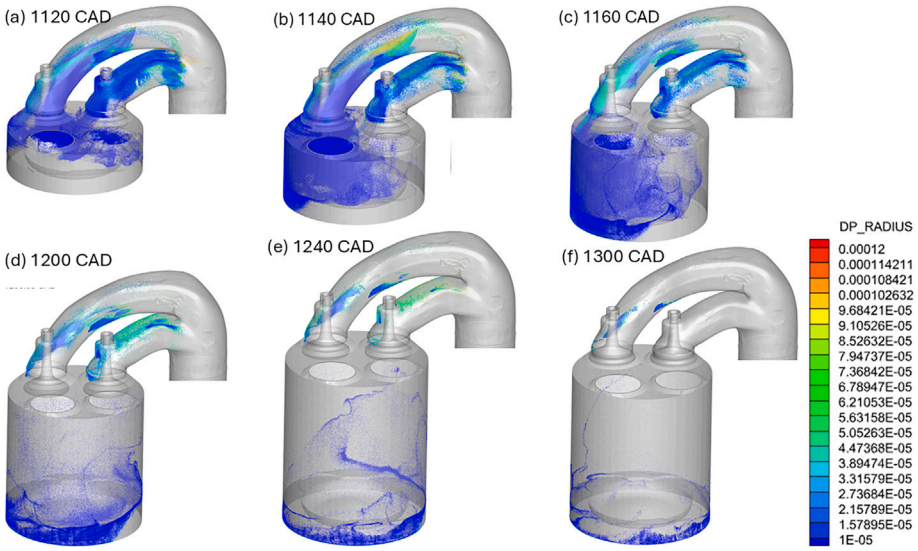

Fig. 29. Evolution of parcels radius in case 25% of total injection amount from short runner.

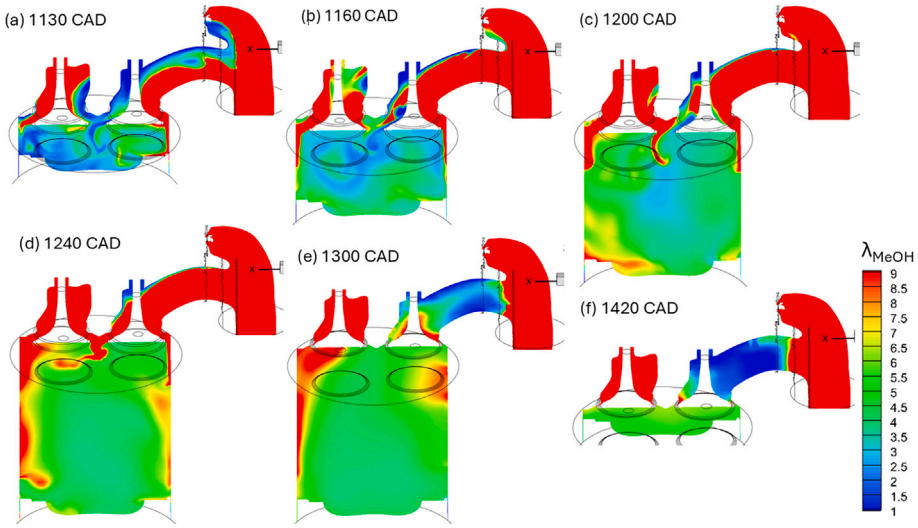

Fig. 30. Distribution of λ_{MeOH} across the intake valves in case 75% of total injection amount from short runner.

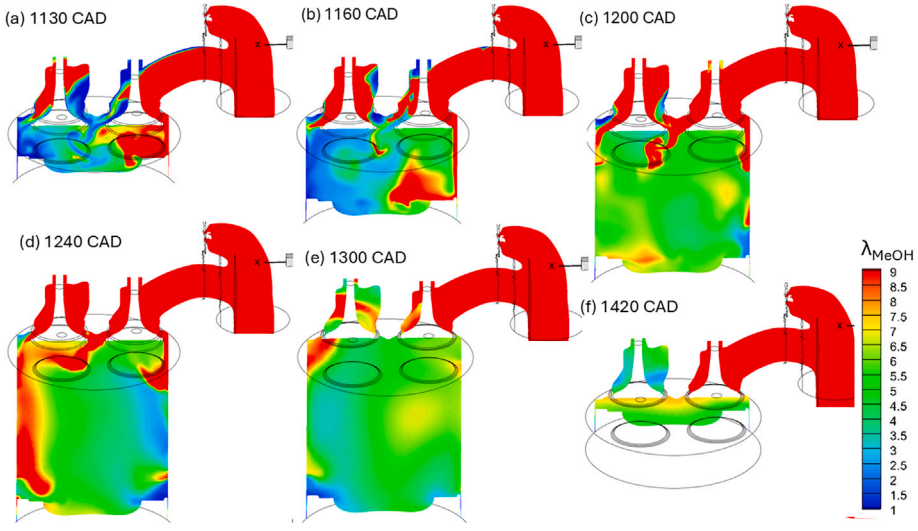

Fig. 31. Distribution of λ_{MeOH} across the intake valves in case 25% of total injection amount from short runner.

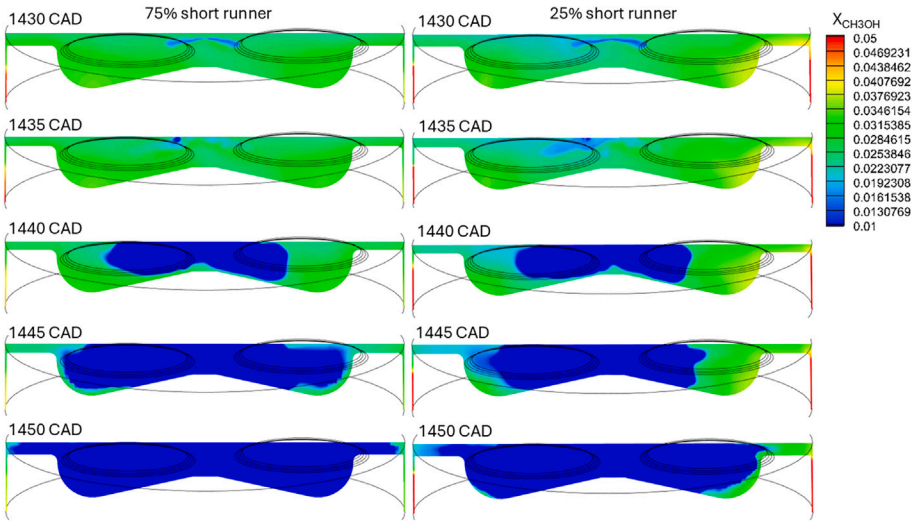

Fig. 32. Distribution of methanol mass fraction in the cylinder from 1430 to 1450 CAD for 75% (the left column) and 25% (the right column) of total injection from short runner.

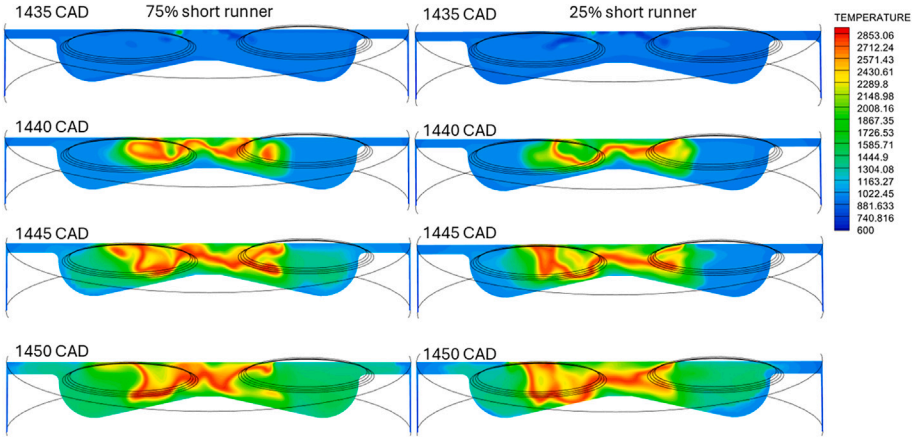

Fig. 33. Temperature field in the cylinder from 1435 to 1450 CAD for 75% (the left column) and 25% (the right column) of total injection from short runner.

bowl on the right is lower than the other side in case of 25% short runner injection. Following the ignition, the unburned temperature on the left side is always higher than the right side in the case of 25% short runner, resulting in faster propagation on one side. The non-uniform temperature field might be attributed to the non-simultaneous and slow droplet evaporation in the cylinder. It takes more time for methanol droplets to reach the right side of the cylinder after EOI, while some remain trapped in the crevice area. This delays evaporation and extends the cooling effect on the air-fuel mixture inside the cylinder. In case of 75% of total injection mass from the short runner, a higher and more evenly distributed temperature field results in a faster burning rate, increasing NOx emissions.

Overall, injecting more methanol from the short runner promotes fuel-air mixture homogeneity and burning rate. This is due to more evenly distributed and faster evaporation of liquid droplets in the cylinder following SOI. In case of homogeneous methanol-air mixture, shorter combustion duration, enhanced combustion and thermal efficiency, low CO emissions, yet higher NOx emissions were observed.

5. Conclusions

The present work successfully investigated the effects of methanol injection amount, timing, and location on mixture formation and combustion of a single cylinder PFI methanol-diesel marine engine. Multi-cycle simulations were conducted incorporating spray modeling and combustion kinetics of both fuels, explicitly taking into account the methanol mixture preparation physics for high-pressure PFI injections. The model was validated using experimental data for both diesel-only and methanol-diesel operation under a low load condition. Using the validated model, a sensitivity analysis including blending ratio (BR), start of injection (SOI) for PFI methanol, and injection location between the two intake runners was conducted. The conclusions drawn from the present investigation are as follows:

(1) As BR varies between 45 and 65%, combustion efficiency ranged between 91.9%–94.8%, while gross ITE ranged between 46.2%–47.3%. Concentration of CO increased by 1.7 times while NOx decreased by 4.2 times with BR increasing from 45% to 75%. Very high BR beyond 65% was not recommended at this low load operation due to low efficiency at BR 75% and partial burn at BR 85%.

(2) Within methanol SOI sweep 300 – 540 CAD, the most uniform mixture and the most rapid flame propagation were found at the earliest injection timing. However, case of SOI 300 CAD resulted in the highest NOx emissions and highest rate of pressure and AHRR rise. In general, as SOI was delayed by 60 CA, efficiency and NOx concentration decreased, while CO emissions increased, except for SOI at 480 CAD.

(3) Improved mixture homogeneity and faster burning rate were observed as more methanol was injected from the short runner. In cases with 50% to 100% of the total injection amount from the short runner, combustion efficiency increased by 6.6%–8%-points and ITE by 3.3%–4.3%-points compared to 0% and 25% from the short runner injection. As short runner injection mass rose from 25% to 75% of total, the concentration of NOx grew by 1.5 times due to an evenly distributed high temperature field.

Overall, this study offers valuable insights into the modeling of methanol-diesel engines, potentially aiding the transition to more sustainable marine engines. Future work should address medium and high load engine conditions as an extension of the scope of this work. In addition, efforts will continue to investigate methanol combustion concepts for maritime engines using the single-cylinder platform through experiments and simulations.

CRediT authorship contribution statement

Giang Bùi: Writing – review & editing, Writing -– original draft, Visualization, Validation, Methodology, Investigation, Formal analysis, Data curation, Conceptualization. **Konstantinos Zoumpourlos:** Writing – review & editing, Validation, Software, Methodology, Conceptualization. **Cemil Bekdemir:** Writing – review & editing, Supervision, Resources, Project administration, Funding acquisition, Conceptualization. **Bart Somers:** Writing – review & editing, Supervision, Software, Project administration.

Declaration of competing interest

The authors declare that they have no known competing financial interests or personal relationships that could have appeared to influence the work reported in this paper.

Acknowledgements

The present research is part of the MENENS project (Methanol als Energiestap Naar Emissieloze Nederlandse Scheepvaart). The project is funded by the Netherlands Enterprise Agency (RVO: Rijksdienst voor Ondernemend Nederland) under the grant number MOB21012. This work utilized the Dutch national e-infrastructure with the support of the SURF Cooperative using grant no. EINF-12527. Simulations were also conducted in parallel using the TU-Eindhoven Supercomputer. We would like to thank Convergent Science for providing their software and technical support which greatly contributed to the accomplishment of this research.

Data availability

The data that has been used is confidential.

References

[1] Kessel DG. Global warming—facts, assessment, countermeasures. J Petrol Sci Eng 2000;26(1–4):157–68.
[2] Al-Enazi A, Okonkwo EC, Bicer Y, Al-Ansari T. A review of cleaner alternative fuels for maritime transportation. Energy Rep 2021;7:1962–85.
[3] Maersk. Maersk secures green methanol for maiden voyage of the world's first methanol-enabled container vessel; 2023. https://www.maersk.com/news/articles/2023/06/13/maersk-secures-green-methanol.
[4] Verhelst S, Turner JWG, Sileghem L, Vancoillie J. Methanol as a fuel for internal combustion engines. Prog Energy Combust Sci 2019;70:43–88.
[5] Bayraktar M, Yuksel O, Pamik M. An evaluation of methanol engine utilization regarding economic and upcoming regulatory requirements for a container ship. Sustain Prod Consum 2023;39:345–56.
[6] Bossel U. Well-to-wheel studies, heating values, and the energy conservation principle. In: European Fuel Cell Forum, vol. 22. 2003. p. 1–5.
[7] Vancoillie J. Modeling the combustion of light alcohols in spark-ignition engines, [Ph.D. thesis], Ghent University; 2013.
[8] Zoumpourlos K, Geertsma R, Van De Ketterij R, Coraddu A. Methanol operation in heavy-duty dici dual-fuel engines: investigating charge cooling effects using ECN spray d data. J Eng Gas Turbines Power 2025:1–10. https://doi.org/10.1115/1.4067862
[9] Hamid H, Ali MA. Handbook of MTBE and other gasoline oxygenates. CRC Press; 2004.
[10] Kiouranakis KI, de Vos P, Zoumpourlos K, Coraddu A, Geertsma R. Methanol for heavy-duty internal combustion engines: review of experimental studies and combustion strategies. Renew Sustain Energy Rev 2025.
[11] Dierickx J, Verbiest J, Janvier T, Peeters J, Sileghem L, Verhelst S. Retrofitting a high-speed marine engine to dual-fuel methanol-diesel operation: a comparison of multiple and single point methanol port injection. Fuel Commun 2021;7:100010.
[12] Wang B, Yao A, Yao C, Chen C, Wang H. In-depth comparison between pure diesel and diesel methanol dual fuel combustion mode. Appl Energy 2020;278:115664.
[13] Ma B, Yao A, Yao C, Chen C, Qu G, Wang W, Ai Y. Multiple combustion modes existing in the engine operating in diesel methanol dual fuel. Energy 2021;234:121285.
[14] Karvounis P, Theotokatos G, Patil C, Xiang L, Ding Y. Parametric investigation of diesel–methanol dual fuel marine engines with port and direct injection. Fuel 2025;381:133441.
[15] Wang H, Yao A, Yao C, Wang B, Wu T, Chen C. Investigation to meet China II emission legislation for marine diesel engine with diesel methanol compound combustion technology. J Environ Sci 2020;96:99–108.
[16] Wang Q, Wei L, Pan W, Yao C. Investigation of operating range in a methanol fumigated diesel engine. Fuel 2015;140:164–70.
[17] Li Z, Wang Y, Yin Z, Gao Z, Wang Y, Zhen X. To achieve high methanol substitution ratio and clean combustion on a Diesel/methanol dual fuel engine: a comparison of Diesel methanol compound combustion (dmcc) and direct dual fuel stratification (ddfs) strategies. Fuel 2021;304:121466.
[18] Cung KD, Wallace J, Kalaskar V, Smith III EM, Briggs T, Bitsis Jr DC. Experimental study on engine and emissions performance of renewable diesel methanol dual fuel (rmdf) combustion. Fuel 2024;357:129664.
[19] Zhu Z, Gu H, Zhu Z, Wei Y, Zeng K, Liu S. Investigation on mixture formation and combustion characteristics of a heavy-duty SI methanol engine. Appl Therm Eng 2021;196:117258.
[20] Wei Y, Zhu Z, Liu S, Liu H, Shi Z, Zeng Z. Investigation on injection strategy affecting the mixture formation and combustion of a heavy-duty spark-ignition methanol engine. Fuel 2023;334:126680.
[21] Singh I, Güdden A, Raut A, Dhongde A, Emran A, Sharma V, Wagh S. Experimental and numerical investigation of a single-cylinder methanol port-fuel injected spark ignition engine for heavy-duty applications. SAE Int J Adv Curr Pract Mobil 2024;6(2024–26–0072):2844–57.
[22] Sun Z, Lian Z, Ma J, Wang C, Li W, Pan J. Combustion and emissions optimization of diesel–methanol dual-fuel engine: emphasis on valve phasing and injection parameters. Processes 2025;13(4):1183.
[23] Mousavi SM, Tripathy S, Molander P, Dahlander P. Effects of port-fuel injected methanol distribution on cylinder-to-cylinder variations in a retrofitted heavy-duty diesel–methanol dual fuel engine. Fuel 2025;391:134733.
[24] Guan W, Wang X, Zhao H, Liu H. Exploring the high load potential of diesel–methanol dual-fuel operation with Miller cycle, exhaust gas recirculation, and intake AIR cooling on a heavy-duty diesel engine. Int J Engine Res 2021;22(7):2318–36.
[25] Han G, Yao A, Yao C, Wu T, Wang B, Wei H. Mechanism analysis on controllable methanol quick combustion. Appl Energy 2017;206:558–67.
[26] Xu C, Zhuang Y, Qian Y, Cho H. Effect on the performance and emissions of methanol/diesel dual-fuel engine with different methanol injection positions. Fuel 2022;307:121868.
[27] Wu T, Yao A, Yao C, Pan W, Wei H, Chen C, Gao J. Effect of diesel late-injection on combustion and emissions characteristics of diesel/methanol dual fuel engine. Fuel 2018;233:317–27.
[28] Wei H, Yao C, Pan W, Han G, Dou Z, Wu T, Liu M, Wang B, Gao J, Chen C, et al. Experimental investigations of the effects of pilot injection on combustion and gaseous emission characteristics of diesel/methanol dual fuel engine. Fuel 2017;188:427–41.
[29] Chen Z, Yao C, Yao A, Dou Z, Wang B, Wei H, Liu M, Chen C, Shi J. The impact of methanol injecting position on cylinder-to-cylinder variation in a Diesel methanol dual fuel engine. Fuel 2017;191:150–63.
[30] Zoumpourlos K, Bekdemir C, Geertsma R, van de Ketterij R, Coraddu A. CFD modeling approach for late-injection methanol sprays validated with ECN spray m. Int J Engine Res 2025:14680874251323931.
[31] Zoumpourlos K, Bekdemir C, Geertsma R, van de Ketterij R, Coraddu A. Methanol sprays in marine engines: CFD modelling of port fuel injection systems. J Mar Eng Technol 2025:1–17.
[32] Kiouranakis KI, Willems R, de Vos P, Geertsma R. Combustion mode analysis of a large-bore methanol premixed dual-fuel engine with high methanol energy fractions. Energy Convers. Manag. X 2025:101417.
[33] Richards KJ, Senecal PK, Pomraning E. Converge 3.0, vol. 540. Madison, WI: Convergent Science; 2021.
[34] Han Z, Reitz RD. Turbulence modeling of internal combustion engines using RNG κ-ε models. Combust Sci Technol 1995;106(4–6):267–95.
[35] Reitz RD, Diwakar R. Structure of high-pressure fuel sprays. SAE Trans 1987:492–509.
[36] Beale JC, Reitz RD. Modeling spray atomization with the Kelvin-Helmholtz/Rayleigh-Taylor hybrid model. At Sprays 1999;9(6).
[37] Schmidt DP, Rutland CJ. A new droplet collision algorithm. J Comput Phys 2000;164(1):62–80.
[38] Post SL, Abraham J. Modeling the outcome of drop–drop collisions in diesel sprays. Int J Multiphase Flow 2002;28(6):997–1019.
[39] Kuhnke D. Spray/wall-interaction modelling by dimensionless data analysis. (no title). 2004.

[40] Curran HJ, Gaffuri P, Pitz WJ, Westbrook CK. A comprehensive modeling study of n-heptane oxidation. Combust Flame 1998;114(1–2):149–77.
[41] Liu S, Sun T, Zhou L, Jia M, Zhao W, Wei H. A new skeletal kinetic model for methanol/n-heptane dual fuels under engine-like conditions. Energy 2023;263:125648.
[42] Heywood J. Internal combustion engine fundamentals. 2018.
[43] Li G, Zhang C, Li Y. Effects of diesel injection parameters on the rapid combustion and emissions of an hd common-rail diesel engine fueled with diesel-methanol dual-fuel. Appl Therm Eng 2016;108:1214–25.
[44] Liu J, Yao A, Yao C. Effects of diesel injection pressure on the performance and emissions of a hd common-rail diesel engine fueled with diesel/methanol dual fuel. Fuel 2015;140:192–200.
[45] Wei L, Yao C, Han G, Pan W. Effects of methanol to diesel ratio and diesel injection timing on combustion, performance and emissions of a methanol port premixed diesel engine. Energy 2016;95:223–32.
[46] Tao W, Sun T, Guo W, Lu K, Shi L, Lin H. The effect of diesel pilot injection strategy on combustion and emission characteristic of diesel/methanol dual fuel engine. Fuel 2022;324:124653.